Northumbria Research Link

Northumbria University
NEWCASTLE

UniversityLibrary

Flexible virtual sensor array based on laser-induced graphene and MXene for detecting volatile organic compounds in human breath

Dongsheng Li[a], Yuzhou Shao[b], Qian Zhang[a], Mengjiao Qu[a], Jianfeng Ping[b], Yongqing Fu[c], Jin Xie[a],*

[a] State Key Laboratory of Fluid Power and Mechatronic Systems, Zhejiang University, Hangzhou, Zhejiang 310027, China

[b] Laboratory of Agricultural Information Intelligent Sensing, School of Biosystems Engineering and Food Science, Zhejiang University, Hangzhou, Zhejiang 310058, China

[c] Faculty of Engineering and Environment, University of Northumbria, Newcastle upon Tyne NE1 8ST, UK

Corresponding author: Jin Xie

Email: xiejin@zju.edu.cn

Abstract. Detecting volatile organic compounds (VOCs) in human breath is critical for early diagnosis of diseases. Good selectivity of VOCs sensors is crucial for accurate analysis of VOCs biomarkers in human breath, which consists of more than 200 types of VOCs. In this paper, a flexible virtual sensor array (FVSA) was proposed based on a sensing layer of MXene and laser-induced graphene interdigital electrodes (LIG-IDEs) for detecting VOCs in the exhaled breath. Fabrication of LIG-IDEs avoids the costly and complicated procedures for preparation of traditional IDEs. The FVSA's responses of multi-parameters build a unique fingerprint for each VOC, without a need for changing the temperature of sensing element, which is commonly used in the VSA of semiconductor VOCs sensors. Based on machine learning algorithms, we have achieved highly precise recognitions of different VOCs and mixtures, and accurate prediction (accuracy of 89.1%) of the objective VOC's concentration in variable backgrounds using this proposed FVSA. Moreover, blind analysis validates the capacity of the FVSA to identify alcohol content in human breath with an accuracy of 88.9%, using breath samples from volunteers before and after alcohol consumption. These results show the proposed FVSA is promising for detection of VOCs biomarkers in human exhaled breath and early diagnosis of the disease.

Keywords: Flexible VOCs sensor; Laser-induced graphene; MXene; Selectivity; Virtual sensor array; Human breath detection;

1. Introduction

Gas sensing is essential for many fields such as agriculture/planting, pollution monitoring, food storage, and medical diagnosis.[1-3] In particular, detecting volatile organic compounds (VOCs) in human breath is considered to be a promising approach for diagnosis of diseases due to its advantages of fast and non-invasive operation as well as requiring no specialized personnel.[4, 5] Approximately 200 VOCs have been detected in human breath and the levels of these VOCs reflect the physical condition of a person.[6] For example, the concentrations of H_2S and NO in the exhaled breath of patients with halitosis and asthma exceed more than several parts per million (ppm)and hundreds of parts per billion (ppb), respectively.[7] Accordingly, VOCs sensors need not only to sensitively detect individual VOCs but also to effectively identify different types of VOCs and quantify the target VOCs in complex backgrounds.

Recent advances in flexible electronics facilitate the development of flexible VOCs sensors that provide real-time information about human breath.[8, 9] Flexible sensors are bendable, easy to wear, and can be attached to various irregular surfaces, which are very convenient for detection of human breath. Nevertheless, the time-consuming and complicated preparation process hinders the large-scale production of these flexible VOCs sensors.[10] Recently, laser-induced graphene (LIG) with porous structure has become a promising material for flexible electrodes.[11, 12] Typically, the LIG is fabricated by converting sp^3 carbon in polyimide (PI) into highly conductive sp^2-hybridized carbon through laser induction. The process combines graphene synthesis and graphene electrode fabrication into one simple process, which can be performed under an ambient atmosphere without using any solvents.

Typically, a sensing material is deposited on the surface of the VOCs sensor and the response of the sensor is greatly dependent on the properties of this sensing layer. Two-dimensional (2D) materials are among the most promising materials for VOCs sensing applications, because of their advantages of large surface area, versatile surface chemistry, and capability of sensitive detection at room temperature.[13, 14] Recently, VOCs sensors based on a new family of 2D materials called MXene have also shown promising performance for application.[15, 16] MXenes possess a metallic conductivity, while their surfaces are covered with many types of functional groups. Among them, $Ti_3C_2T_x$-based VOCs sensors were reported to have ultra-high signal-to-noise ratios and low limit of detections compared with VOCs sensors based on other types of 2D materials.[17] However, MXenes have strong adsorptions to various VOCs, and thus how to improve the selectivity of the MXene-based VOCs sensors remains a key challenge.

Combining sensors into arrays is an effective approach to enhance the poor selectivity of each individual sensor, and this is sometimes referred to as an "electronic nose" or e-nose.[18-20] However, multi-

sensor systems often face many issues, such as high power consumption, complicated sensing circuits, and high breakdown possibilities, since the whole e-nose system does not work if any of the component sensors fails.[21]

To overcome the drawbacks of conventional sensor arrays, virtual sensor array (VSA) was proposed, which means a single VOCs sensor can produce a multi-dimensional signal similar to that generated by an electronic nose.[22-24] For the VSA, multi-dimensional responses are usually analyzed using machine learning techniques, such as principal component analysis (PCA),[25] linear discriminant analysis (LDA),[26] and partial least squares (PLS).[27] For semiconductor VOCs sensors, changing the temperature of sensing elements is one of the most commonly used methods in reported VSAs to mitigate the poor selectivity.[28] For example, Tonezzer *et al.* proposed a VSA by varying the temperature of $Pt-SnO_2$ nanowires for selective detection of VOCs.[29] However, the time to reach the targeted temperature is often too long for many real applications and high temperature may cause permanent changes of the sensing layer's properties. In the previous work, we proposed a VSA based on impedance spectra for selective detecting VOCs without the need to change the temperature of sensing element.[30]

In this paper, we present a flexible VSA (FVSA) based on LIG interdigital electrodes (LIG-IDEs) and a sensing layer of MXene, as schematically illustrated in Figure 1. The FVSA can produce a multi-dimensional response which resemble that generated by an electronic nose. In this method, we deposited a $Ti_3C_2T_x$ film on the surface of LIG-IDEs to form a FVSA, which was then exposed to different concentrations of multiple VOCs at room temperature. The broadband impedance spectra of the FVSA were measured under various conditions and we extract characteristic parameters from them. A systematic analysis of the characteristic parameters was carried out using machine learning algorithms to identify different types of VOCs and predict the concentration of the target VOC in various backgrounds. In addition, the FVSA was used to identify alcohol content in human breath samples. To our knowledge, this is the first report using a FVSA to detect VOCs in human exhaled breath. This paper is an extension work of a conference paper.[31]

2. Experimental

2.1 Fabrication and characterization of the FVSA.

The sensor was fabricated by coating a layer of $Ti_3C_2T_x$ on the prepared LIG-IDEs. In the $Ti_3C_2T_x$ structure, two layers of carbon atoms are sandwiched between three layers of titanium, and the surface of $Ti_3C_2T_x$ is terminated by fluorine ($-F$), oxygen ($-O$), and hydroxyl ($-OH$) groups.[32] The detailed synthesis
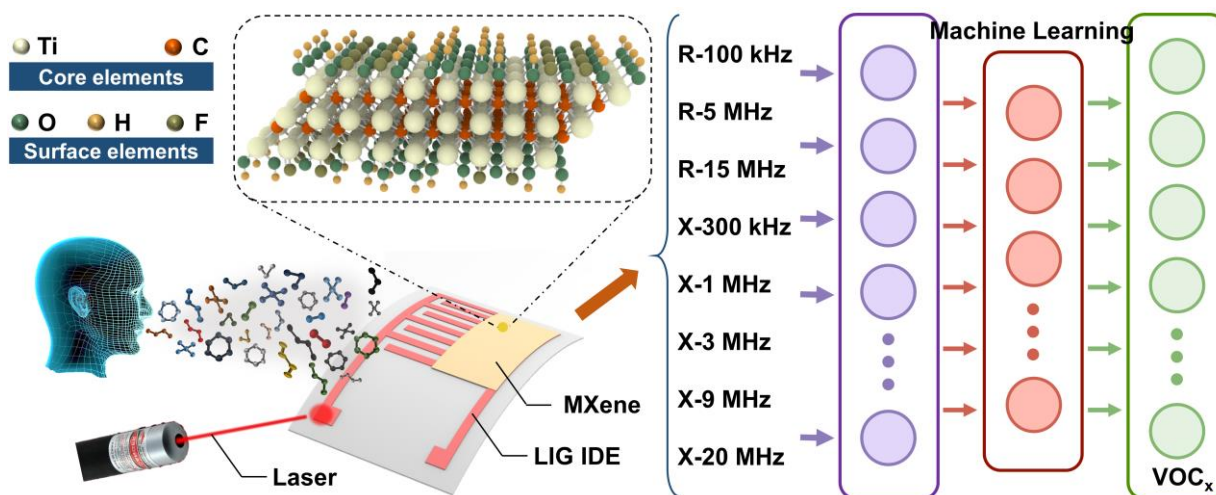
Figure 1. Schematic illustration of the of the FVSA.

process of $Ti_3C_2T_x$ is shown in S1 of supplementary information. The flexible LIG-IDEs consist of three layers: LIG on the top, PI tape in the middle, and PI film as the supporting substrate. The laser direct writing technology was adopted with for PI patterning. The scan speed and laser power of the direct writing are 2 cm·s⁻¹ and 3.85 W, respectively. The length and width of the LIG-IDE are 13.3 mm and 12 mm respectively, which is composed of six pairs of electrodes. The length and width of the electrodes are 9 mm and 500 μm. The gap between the electrodes and the length of opposite electrode are 300 μm and 8 mm. A dispersion of $Ti_3C_2T_x$ at a concentration of 0.5 mg/mL in deionized water (100 μL) was dropped on the fabricated LIG-IDEs. After being dried, the sensing layer formed. Characterization methods of the FVSA have been presented in S2 of supplementary information.

2.2 VOCs exposure.

Figure S1 shows the schematic illustration of VOCs sensing experimental setup. Firstly, the performance of the FVSA was studied by exposing the FVSA to different concentrations of multiple VOCs and VOCs mixtures. The broadband impedance spectra (frequency range from 30 kHz to 30 MHz) were measured using a network analyzer (Agilent, E5061B). Response was defined as the relative change in impedance relative to the baseline impedance after VOCs exposure (i.e., $\Delta R (X) / R_0 (X_0)$) (%). Response and recovery time were defined as the time from when the impedance starts to change until the impedance reaches 90% of its final value. The capabilities of the proposed FVSA were tested to identify the alcohol content in 36 real exhalation samples. 18 volunteers were asked to drink 100 ml of beer with an alcohol content of 2.5%vol to 3%vol. Breath samples were collected from each volunteer before and 30 minutes after alcohol consumption. The test temperature was maintained at a room temperature (25℃).

2.3 Data Analysis.

Three sensors were tested under same conditions, and results were expressed using the mean value ±

its standard deviation. Reactance is defined as the imaginary part of impedance. Eight characteristic parameters from broadband impedance spectrum of the FVSA are used to build VOCs classification and concentration prediction models. They are the resistances at 100 kHz, 5 MHz, 15 MHz and the reactances at 300 kHz, 1 MHz, 3 MHz, 9 MHz, 20 MHz respectively. Detailed data analysis method is shown in S3 of supplementary information.

3. Results and discussion

3.1 Material Characterizations.

Figure 2a shows the prepared flexible LIG-IDEs with a good flexibility. Figure 2b shows an SEM image of the fabricated LIG-IDEs with consistent line widths and sharp edges, revealing the successful processing of LIG-IDEs by laser direct writing technology. The ordered porous surface morphology of the prepared LIG-IDEs is shown in Figure 2c. Figure 2d shows a cross-sectional SEM image of the obtained LIG-IDEs, revealing the three-layer structure of PI film, PI tape and LIG. Figure 2e shows an image of MXene-based flexible VOCs sensor after coated with a uniform $Ti_3C_2T_x$ film (Inset: a photograph of the LIG-IDEs). The elemental maps (Figure 2f) reveal uniform distributions of core elements (C, Ti) and surface elements (O, F), indicating a good surface functionality.

Figure S2 shows SEM and TEM images of $Ti_3C_2T_x$ nanosheets, indicating that the average lateral size of the $Ti_3C_2T_x$ nanosheets is about 1.5 μm. SEM images of the proposed sensor with $Ti_3C_2T_x$ film are shown in Figure S3. Figure S3b shows the SEM image of $Ti_3C_2T_x$ film in the channel (i.e., on top of PI). Figure S3c shows the surface SEM image of LIG-IDEs after coating with $Ti_3C_2T_x$. No $Ti_3C_2T_x$ film on the IDEs can be observed. Because the thickness of the LIG-IDEs is much larger than that of the $Ti_3C_2T_x$ film and the surface of LIG-IDEs is porous and uneven. Figures S3d-f show the cross-sectional SEM image of the flexible sensor (in the channel) and its corresponding elemental mapping analysis results (Ti and O). The thickness of $Ti_3C_2T_x$ film is ~1.2 μm. The resistance values of the flexible VOCs sensor and LIG-IDEs are rather stable even after 1000 cycles of bending, as shown in Figure S4, revealing high mechanical strength and good flexibility of the VOCs sensor based on $Ti_3C_2T_x$ film and LIG-IDEs. The resistance of LIG-IDEs increases slightly after 1000 cycles due to the formation of microcracks caused by the repeated applied strain.

Raman spectrum of the LIG shows three main peaks: the first-order D peak (roughly at 1350 cm^{-1}), the first-order G peak (roughly at 1580 cm^{-1}), and the second-order D peak (roughly at 2660 cm^{-1}), as shown in Figure 2g. It confirms successful fabrication of high-quality LIG-IDEs using laser direct writing
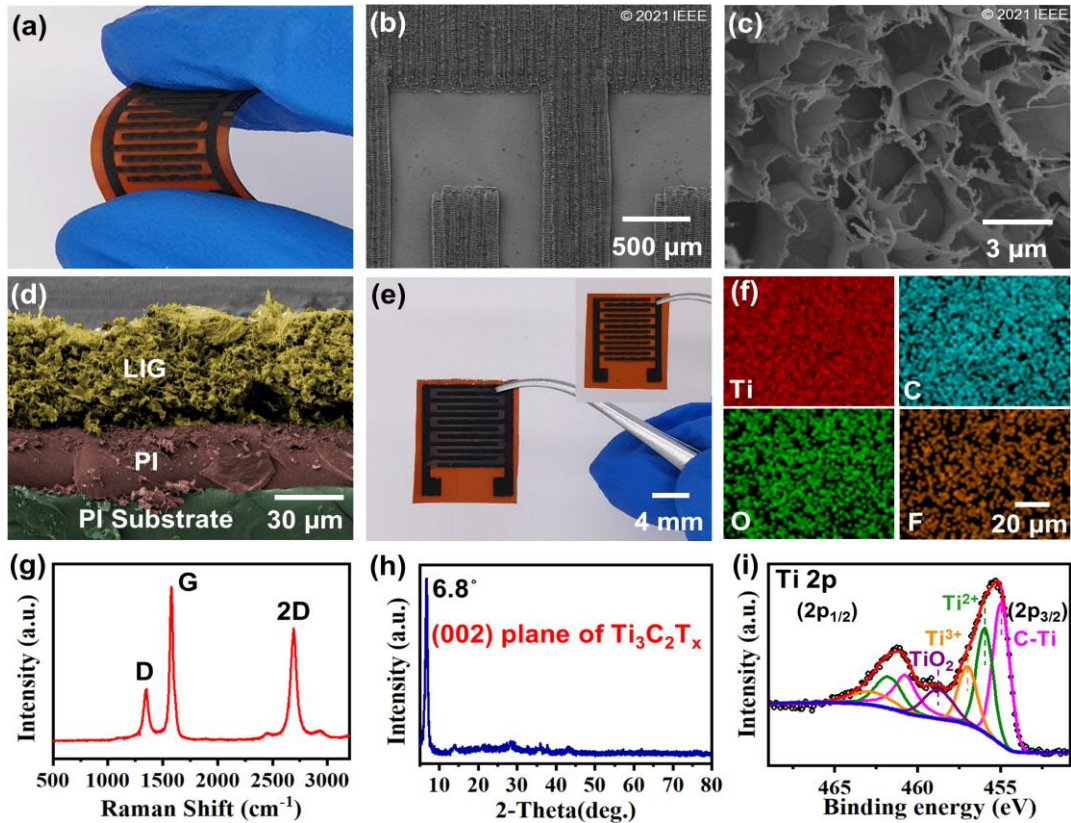
6

Figure 2. Surface and structural characterizations of the PI-based flexible VOCs sensor. (a) Photograph of the PI-based flexible LIG-IDE. (b) SEM image of the PI-based LIG-IDE with finger spacing of 300 μm. (c) Surface morphology of PI-based flexible LIG-IDE (d) Cross-sectional SEM image of the PI-based electrode. (e) Photograph of the flexible sensor after coating with $Ti_3C_2T_x$. Inset: photograph of the LIG-IDE. (f) Elemental mapping analyses of the $Ti_3C_2T_x$ film. (g) Raman spectrum of the flexible LIG-IDE. (h) XRD patterns and (i) XPS (Ti 2p) of $Ti_3C_2T_x$ film.

technology.[33] X-ray diffraction (XRD) curve of the $Ti_3C_2T_x$ film reveals a sharp peak at $2\theta = 6.8°$, indicating that $Ti_3C_2T_x$ was successfully prepared from Ti_3AlC_2, as shown in Figure 2h.[34] This peak corresponds to (002) peak of the $Ti_3C_2T_x$ film, indicating the center-to-center distance of $Ti_3C_2T_x$ is 13 Å. Figures 2i and S4 show high-resolution X-ray photoelectron spectra (XPS) of $Ti_3C_2T_x$ (Ti 2p, C 1s, O 1s). Ti 2p spectrum (Figure 2i) can be deconvoluted into four doublets (Ti $2p_{3/2}$, Ti $2p_{1/2}$) with a doublet separation of 5.8 eV and an area ratio of 2:1. The Ti $2p_{3/2}$ peaks centered at 454.94 eV, 455.94 eV, 456.97 eV, and 458.74 eV are assigned to Ti−C (Ti^+), Ti−X (Ti^{2+}), Ti_xO_y (Ti^{3+}), and TiO_2 (Ti^{4+}), respectively, which is as reported by the previous XPS results.[35] The C 1s spectrum (Figure S5a) shows four types of carbon atoms. Peaks centered at 281.7 eV, 284.8 eV, 285.3 eV, 286.6 eV correspond to C-Ti, C-C, C-O, and O-C=O, respectively. The O 1s spectrum can be deconvoluted into three peaks centered at 529.7 eV, 533 eV, and 533.4 eV, corresponding to TiO_2, Ti-O-Ti, and Ti−OH, respectively, as shown in Figure S5b.[36]

3.2 Dynamic VOCs sensing performance.

Figure S6a shows resistance and reactance responses of the flexible sensor operated at 1 MHz investigated by exposing the VOCs sensor to ethanol with different concentrations from 100 to 800 ppm.

The resistance and reactance of the sensor were continuously measured with an interval of 1 s. Both the resistance and reactance of the sensor show positive increases to ethanol but the increased value of resistance is relatively small. The resistance and reactance baselines of the VOCs sensor drift up slightly, indicating the non-recoverable responses of the $Ti_3C_2T_x$-based sensor, mainly caused by the slow recovery due to chemisorption of ethanol by the $Ti_3C_2T_x$ film. Figure S6b shows the short-term repeatability of the sensor upon exposure to ethanol vapors with concentration of 100 ppm for four consecutive cycles, indicating the good repeatability of the sensor. The response and recovery speeds of the proposed sensor were further investigated, and the detailed response and recovery processes of the sensor are shown in Figures S5c and S5d. Interestingly, the response and recovery times of resistance are different from those of reactance. The response times of resistance and reactance responses are 33 s and 17 s and the recovery times of resistance and reactance responses are 35 s and 67 s, respectively. The reason for this phenomenon is that the resistance and reactance at 1 MHz are dominated by the different properties of the $Ti_3C_2T_x$ film, and response and recovery times of different properties are different upon exposure to ethanol, which will be discussed in the next section. Figure S7 shows impedance responses of the flexible sensor operated at 1 MHz upon exposure to different VOCs, i.e., 100 ppm of methanol (MeOH), ethanol (EtOH), acetone, and isopropanol (IPA). The impedance values show positive changes after VOCs exposure.

3.3 VOCs fingerprints and working principle.

The $Ti_3C_2T_x$ based VSA was exposed to four types of vapors, i.e., from 100 ppm to 800 ppm of MeOH, EtOH, IPA, and acetone. The impedance spectra (frequency range from 30 kHz to 30 MHz) of the FVSA were obtained in the context of different VOCs. Eight representative parameters are selected as the VOCs characteristics based on the obtained impedance spectra, as mentioned above. A fingerprint for each VOC can be created by the multi-dimensional responses based on relative changes of all the eight characteristics, as shown in Figure S8. Different VOCs generate different response patterns, which allows a straightforward discrimination of different types of VOCs. Resistance value at 15 MHz exhibits a negative change, whereas the other characteristic parameters exhibit positive changes upon exposure to various VOCs. To visualize the unique response patterns of the multiple VOCs, relative changes of all eight characteristic parameters are plotted as radar plots after VOCs exposure., which is shown in Figure 3a. Apparently, different VOCs have different fingerprints. Therefore, we determine that a unique fingerprint for each VOC can be created by the multi-parameter sensing responses.

Figure 3b shows the experimental Nyquist curve of the FVSA over a frequency range of 30 kHz-30 MHz in dry air. We fit the curve to obtain the equivalent circuit model. The fitting data are very close to
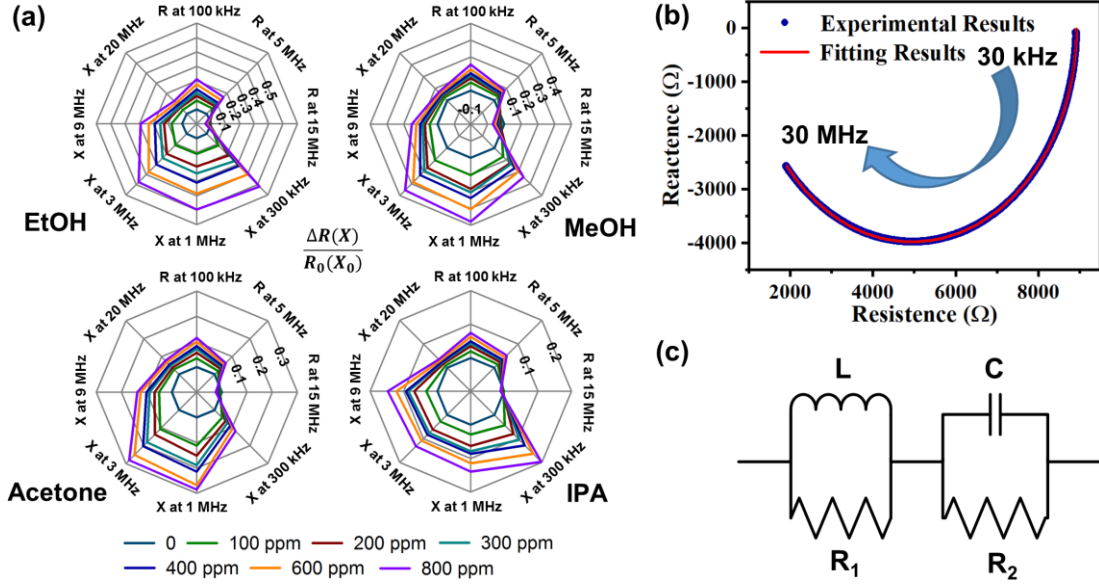
Figure 3. VOCs fingerprints and the equivalent circuit model of the FVSA. (a) Radar plot of unique fingerprint patterns of different VOCs. (b) Experimental Nyquist curve and fitting curve. (c) The equivalent circuit model of the FVSA.

the experimental data, indicating the equivalent circuit model with high accuracy. The equivalent circuit model of the FVSA is shown in Figure 3c. Here the circuit elements *R1* and *L* represent the resistance in thickness direction and inductance between $Ti_3C_2T_x$ layers, and elements *R2* and *C* represent the transverse resistance and capacitance between electrodes.[37, 38] The contact resistance between the LIG-IDEs and the $Ti_3C_2T_x$ film can be neglected. The values of *R1*, *L*, *R2*, *C* are 969.3 Ω, $1.396 \cdot 10^{-5}$ H, 8923.3 Ω, $1.63 \cdot 10^{-12}$ C, respectively. In the circuit model, the AC resistance (*R(f)*) and reactance (*X(f)*) can be written as

$$R(f) = \frac{(2\pi f)^2 L^2 R1}{R1^2 + (2\pi f)^2 L^2} + \frac{R2}{1 + (2\pi f)^2 C^2 R2^2} \tag{1}$$

$$X(f) = \frac{2\pi f L R1^2}{R1^2 + (2\pi f)^2 L^2} - \frac{2\pi f C R2^2}{1 + (2\pi f)^2 C^2 R2^2} \tag{2}$$

Various effects lead to impedance changes of the MXene-based sensor and the proportions of multiple effects caused by different VOCs are quite different.[15-17, 39] These effects lead to changes of the sensor properties, such as transverse resistance and capacitance between electrodes, which correspond to components in the equivalent model of the sensor. So each VOC has an effect of specific proportion on multiple components in the equivalent circuit model.[40, 41] The impedance obtained at each frequency is determined by all components in the equivalent model and the influences of changes of every component on impedances (*R(f)* and *X(f)*) are affected by frequency, which is shown clearly in Eqs. (1) and (2). If the influences of two VOCs on each component in the equivalent model are not the same, the changes of

impedance spectra will be different after exposure to VOCs. Therefore, VOCs fingerprints can be generated using the multi-parameter sensing responses based on the broadband impedance spectra.

3.4 VOCs identification and concentration prediction.

In order to qualitatively discriminate various VOCs with the similar properties and define the dimensionality of the of the FVSA's responses after VOCs exposure, the matrix of characteristic parameters variations was analyzed by PCA, which consists of 24 rows (four VOCs with six different concentrations) and 8 columns (characteristic parameters). After the PCA transformation, the percentage of cumulative variance of the first three principal components (PCs) exceeds 98%. The variance percentages for PC1-PC3 are 87.16%, 9.6% and 2.6%, respectively. Therefore, high data dimensionality of FVSA's responses is achieved after exposure to only four VOCs.

The scores of obtained first three PCs are depicted into a 3D plot, as shown in Figure 4a. Points with different color correspond to different types of VOCs and each point denotes a VOCs fingerprint at a certain concentration. Points denoting different types of VOCs are dispersed in space, and points denoting the same VOC (from 100 ppm to 800 ppm) are situated roughly on a line, indicating the capability of the FVSA to identify different types of VOCs.

Then the LDA performed was carried out to quantitatively identify different VOCs. A 3D plot of LDA scores of various VOCs is shown in Figure 4b. Points with different color correspond to different types of VOCs. A pentagram is the mass center of each point group denoting the same VOC. Various types of VOCs can be well discriminated. Figure 4c shows the LDA results for VOCs identification. Each VOC sample was identified correctly with an accuracy of 100%. The leave-one-out cross validation (LOOCV) was performed to investigated the validity of LDA model. Cross-validation correct rate is 95.8%, indicating that one out of 24 samples is misclassified, which is shown in Figure 4d.

In order to further investigate the discriminating power of the FVSA, we exposed the FVSA toward similar complex VOCs mixtures, in which A, B, C, D are mixtures of EtOH and MeOH, EtOH and IPA, EtOH and acetone, as well as EtOH and dichloromethane, respectively. The concentrations of mixtures during the test are listed in Table S1. We carried out the LDA to identify the FVSA's responses after VOCs mixtures exposure. Figure 4e shows a plot in a 3D feature space for identification of VOCs mixtures. Four VOCs mixtures are well separated from different angles of view. 100% correct prediction means that the mixtures with various concentrations are identified as the correct mixture type. As shown in Figure 4f, the correct classification rate is 85%. Figure 4g shows the corresponding LOOCV results, indicating the

correct cross-validation rate of identification for VOCs mixtures is 85%. These results indicate that the proposed FVSA has capability for identification of both pure VOCs and similar VOCs mixtures.
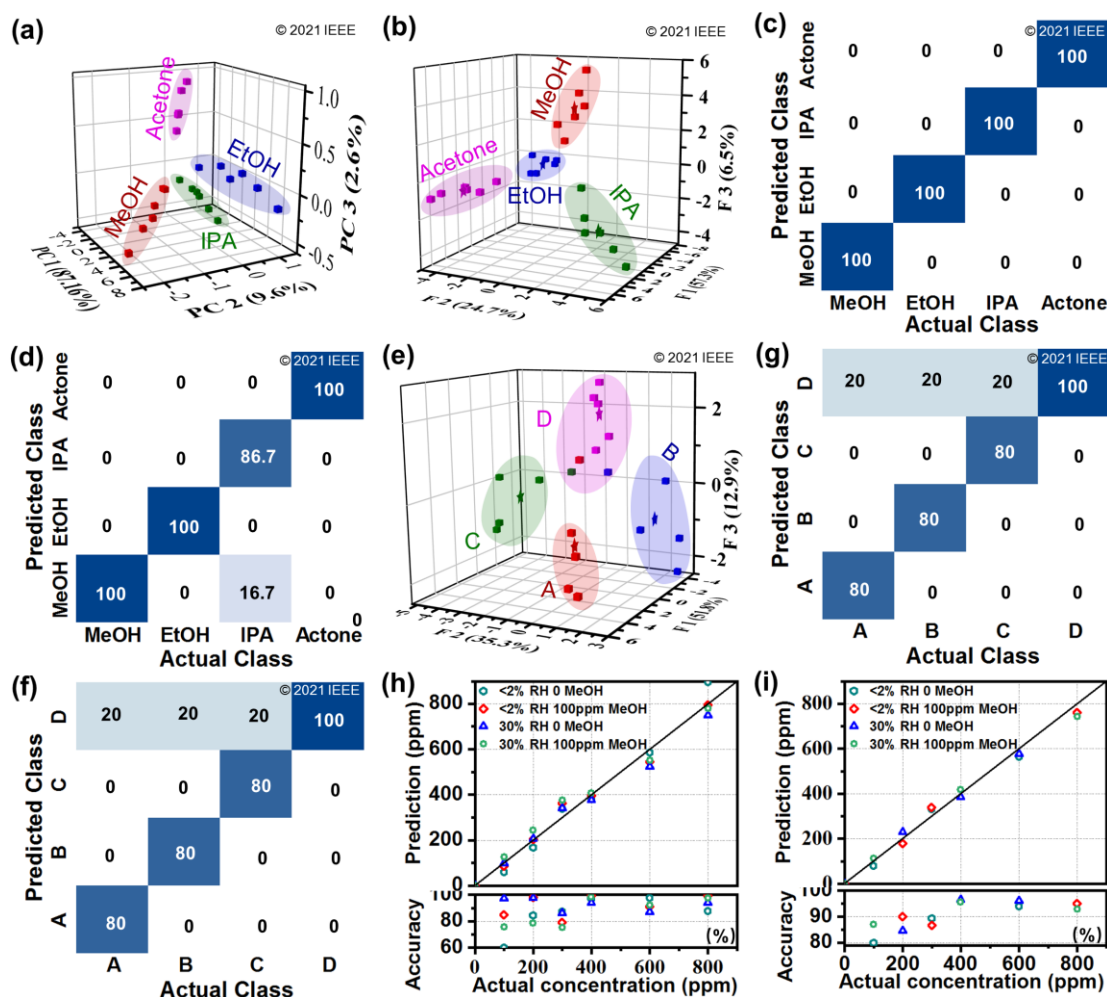

Figure 4. Results of VOCs identification and concentration prediction. (a) 3D plot of the first 3 principal components of PCA results of different VOCs. 3D plot of LDA results the four VOCs (b) and VOCs mixtures (e). Identification results of four VOCs (c) and VOCs mixtures (f). Cross-validation results of identification of four VOCs (d), and VOCs mixtures (g). (h) Ethanol concentration prediction in the presence of a variable background. (i) Concentration prediction of second data set.

Figure S9 shows the responses of the sensor to ethanol in different backgrounds. The impedance of the sensor in dry air is chosen as the zero point. The $Ti_3C_2T_x$-based sensor has drifts when the ethanol concentration is zero in the presence of methanol and water because $Ti_3C_2T_x$ also absorbs methanol and water.[17, 39] The response of the FVSA is not a linear superposition of the response to water or methanol and the response to ethanol. This is because the adsorption sites for ethanol are partially occupied by water or methanol. Therefore, we cannot eliminate the influence of humidity or methanol through detecting a single parameter.

PLS regression analysis was performed to quantify concentrations of EtOH in various backgrounds with different humidity levels and MeOH concentrations. Four latent variables (LVs) were selected to

provide the minor prediction error without generating an overfitting, based on the root of sum of squared error (SSE) and average accuracy of prediction as a function of LV number as shown in Figure S10. Figure 4h presents the results of the prediction for EtOH concentration in various backgrounds with different humidity levels and MeOH concentrations. In principle, if the prediction matches the real EtOH concentration, then the corresponding point is located on diagonal line. As shown in Figure 4h, all points are approaching the diagonal, indicating the ethanol concentrations are predicted quite well. An average accuracy of 89.1% for EtOH concentration prediction is achieved. In order to investigate the reliability of the prediction model, a second dataset was employed as input for the PLS model built from previous dataset. Figure 4i shows a concentration prediction of second dataset. As illustrated, ethanol concentrations are predicted quite well, demonstrating that the LIG-based FVSA is suitable for the concentration prediction of target VOC in variable backgrounds.

3.5 Human exhalation detection.

The FVSA based on MXene and LIG electrodes were used for frequency and composition analysis of human exhalation. As shown in Figure 5a, the FVSA is integrated into a medical breathing mask for monitoring human respiration in real time, Figures 5b and 5c show the resistance and reactance responses of the FVSA operated at 1 MHz for human breathing. One breathing period involves two actions: exhalation and inhalation. In the exhalation process, the resistance and reactance increase quickly, mainly due to the water and heat in exhalation as well as force produced by airflow.[42, 43] The resistance and reactance then return back to their normal values during the inhalation process. The periodic changes of resistance and reactance are obviously different upon exhalation. The reason for this phenomenon is that the resistance and reactance are dominated by different components in the equivalent circuit, i.e., different properties of the sensing film, whose change processes are different after exposure to exhalation.

In addition, we investigated the capacity of the FVSA to identify whether a person consumes alcohol based on the multi-parameter responses. The FVSA was exposed to 36 real breath samples collected from 18 volunteers before and after alcohol consumption.[44] LDA was employed for discrimination of these samples. Figure 5d shows the identification results of breath samples. An accuracy of 94.4% was achieved via LDA identification, indicating that 2 out of 36 samples were misclassified. The misclassified samples are indicated by points marked by circles. LOOCV was performed to tested the validity of the identification. The correct cross-validation rate is 88.9%. The two samples misclassified in LOOCV are indicated by the points marked by triangle symbol. Ethanol has effects of unique proportions on components in equivalent circuit model of the FVSA which stand for various properties of MXene.

12

Therefore, using the FVSA based on LIG-IDEs and MXene, we can make accurate judgments about whether a person drinks alcohol or not.
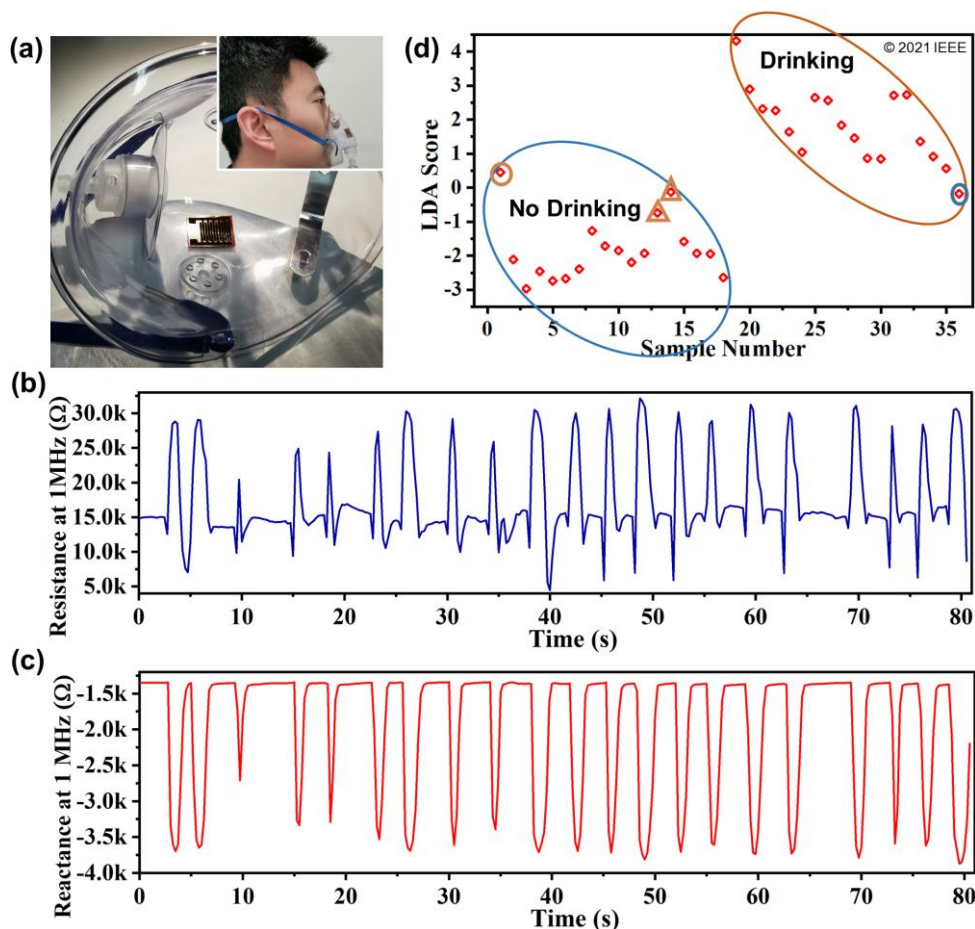

Figure 5. Frequency and composition analysis of human exhalation breath. (a) Photograph of a breathing mask with the LIG-based FVSA fixed inside for breath monitoring, inset shows a volunteer wearing the mask. Resistance (b) and reactance (c) response of the FVSA operated at 1 MHz to human breath. (d) Identification results of whether there is alcohol using breath samples collected from volunteers.

4. Conclusions

In conclusion, we proposed a FVSA based on LIG-IDEs and MXene to detect VOCs in human breath. The fabrication of LIG-IDEs avoids the complicated and costly procedures for preparation of traditional IDEs. We deposited a $Ti_3C_2T_x$ film on the surface of LIG-IDEs to form a FVSA. The FVSA's responses of eight characteristic parameters from broadband impedance spectra create a unique fingerprint for each VOC without a need for changing temperature of the sensor. The identification accuracies for VOCs and VOCs mixtures are 95.8% and 85%, respectively. The prediction accuracy of the ethanol concentration is up to 89.1% in the presence of water and methanol with different concentrations using the proposed FVSA. Blind analysis validates the capability of the FVSA to identify alcohol contents with an accuracy of 88.9%

in real breath samples collected from volunteers before and after drinking. The high level of identification and concentration prediction shows that the proposed FVSA is promising for detection of VOCs biomarkers in human exhaled breath and early diagnosis of the disease.

Author contributions

Dongsheng Li: Conceptualization, Data curation, Formal analysis, Writing - original draft.

Yuzhou Shao: Investigation, Methodology.

Qian Zhang: Software, Methodology.

Mengjiao Qu: Validation, Visualization

Jianfeng Ping: Supervision.

Yongqing Fu: Writing - review & editing, Supervision.

Jin Xie: Project administration, Writing - review & editing, Supervision.

Conflicts of Interest

There are no conflicts to declare.

Acknowledgments

References

(1) Haroun, A.; Le, X.; Gao, S.; Dong, B.; He, T.; Zhang, Z.; Wen, F.; Xu, S.; Lee, C. Progress in micro/nano sensors and nanoenergy for future AIoT-based smart home applications. *Nano Express* **2021,** *2* (2), 022005.

(2) Zhu, J.; Sun, Z.; Xu, J.; Walczak, R. D.; Dziuban, J. A.; Lee, C. Volatile organic compounds sensing based on Bennet doubler-inspired triboelectric nanogenerator and machine learning-assisted ion mobility analysis. *Science Bulletin* **2021,** *66* (12), 1176-1185.

(3) Potyrailo, R. A.; Go, S.; Sexton, D.; Li, X.; Alkadi, N.; Kolmakov, A.; Amm, B.; St-Pierre, R.; Scherer, B.; Nayeri, M.; Wu, G.; Collazo-Davila, C.; Forman, D.; Calvert, C.; Mack, C.; McConnell, P. Extraordinary performance of semiconducting metal oxide gas sensors using dielectric excitation. *Nat. Electron.* **2020,** *3*, 280-289.

(4) Righettoni, M.; Tricoli, A.; Pratsinis, S. E. Si: WO3 sensors for highly selective detection of acetone for easy diagnosis of diabetes by breath analysis. *Anal. Chem.* **2010,** *82*, 3581-3587.

(5) Kim, S.-J.; Choi, S.-J.; Jang, J.-S.; Kim, N.-H.; Hakim, M.; Tuller, H. L.; Kim, I.-D. Mesoporous WO3 Nanofibers with Protein-Templated Nanoscale Catalysts for Detection of Trace Biomarkers in Exhaled Breath. *ACS Nano* **2016,** *10*, 5891-5899.

(6) Chan, L. W.; Anahtar, M. N.; Ong, T.-H.; Hern, K. E.; Kunz, R. R.; Bhatia, S. N. Engineering synthetic breath biomarkers for respiratory disease. *Nat. Nanotechnol.* **2020,** *15*, 792-800.

(7) Moon, H. G.; Jung, Y.; Han, S. D.; Shim, Y.-S.; Shin, B.; Lee, T.; Kim, J.-S.; Lee, S.; Jun, S. C.; Park, H.-H.; Kim, C.; Kang, C.-Y. Chemiresistive Electronic Nose toward Detection of Biomarkers in Exhaled Breath. *ACS Appl. Mater. Interfaces* **2016,** *8*, 20969-20976.

(8) Wang, B.; Thukral, A.; Xie, Z.; Liu, L.; Zhang, X.; Huang, W.; Yu, X.; Yu, C.; Marks, T. J.; Facchetti, A. Flexible and stretchable metal oxide nanofiber networks for multimodal and monolithically integrated wearable electronics. *Nat. Commun.* **2020,** *11*, 2405: 1-11.

(9) Huang, X.; Li, B.; Wang, L.; Lai, X.; Xue, H.; Gao, J. Superhydrophilic, Underwater Superoleophobic, and Highly Stretchable Humidity and Chemical Vapor Sensors for Human Breath Detection. *ACS Appl. Mater. Interfaces* **2019,** *11*, 24533-24543.

(10) Zhu, J.; Liu, X.; Shi, Q.; He, T.; Sun, Z.; Guo, X.; Liu, W.; Sulaiman, O. B.; Dong, B.; Lee, C. Development Trends and Perspectives of Future Sensors and MEMS/NEMS. *Micromachines* **2020,** *11* (1), 7.

(11) Soares, R. R. A.; Hjort, R. G.; Pola, C. C.; Parate, K.; Reis, E. L.; Soares, N. F. F.; McLamore, E. S.; Claussen, J. C.; Gomes, C. L. Laser-Induced Graphene Electrochemical Immunosensors for Rapid and Label-Free Monitoring of Salmonella enterica in Chicken Broth. *ACS Sens.* **2020,** *5*, 1900-1911.

(12) Lan, L.; Le, X.; Dong, H.; Xie, J.; Ying, Y.; Ping, J., One-step and large-scale fabrication of flexible and wearable

humidity sensor based on laser-induced graphene for real-time tracking of plant transpiration at bio-interface. *Biosens. Bioelectron.* **2020**, *165*, 112360: 1-7.

(13) Liu, X.; Ma, T.; Pinna, N.; Zhang, J. Two-Dimensional Nanostructured Materials for Gas Sensing. *Adv. Funct. Mater.* **2017**, *27*, 1702168: 1-30.

(14) Yuan, W.; Liu, A.; Huang, L.; Li, C.; Shi, G. High-Performance NO2Sensors Based on Chemically Modified Graphene. *Adv. Mater.* **2013**, *25*, 766-771.

(15) Lee, E.; VahidMohammadi, A.; Prorok, B. C.; Yoon, Y. S.; Beidaghi, M.; Kim, D.-J. Room temperature gas sensing of two-dimensional titanium carbide (MXene). *ACS Appl. Mater. Interfaces* **2017**, *9*, 37184-37190.

(16) Wu, M.; He, M.; Hu, Q.; Wu, Q.; Sun, G.; Xie, L.; Zhang, Z.; Zhu, Z.; Zhou, A. Ti3C2 MXene-Based Sensors with High Selectivity for NH3 Detection at Room Temperature. *ACS Sens.* **2019**, *4*, 2763-2770.

(17) Kim, S. J.; Koh, H.-J.; Ren, C. E.; Kwon, O.; Maleski, K.; Cho, S.-Y.; Anasori, B.; Kim, C.-K.; Choi, Y.-K.; Kim, J.; Gogotsi, Y.; Jung, H.-T. Metallic Ti3C2Tx MXene Gas Sensors with Ultrahigh Signal-to-Noise Ratio. *ACS Nano* **2018**, *12*, 986-993.

(18) Fahad, H. M.; Shiraki, H.; Amani, M.; Zhang, C.; Hebbar, V. S.; Gao, W.; Ota, H.; Hettick, M.; Kiriya, D.; Chen, Y. Z. Room temperature multiplexed gas sensing using chemical-sensitive 3.5-nm-thin silicon transistors. *Sci. Adv.* **2017**, *3*, e1602557: 1-8.

(19) Lichtenstein, A.; Havivi, E.; Shacham, R.; Hahamy, E.; Leibovich, R.; Pevzner, A.; Krivitsky, V.; Davivi, G.; Presman, I.; Elnathan, R.; Engel, Y.; Flaxer, E.; Patolsky, F. Supersensitive fingerprinting of explosives by chemically modified nanosensors arrays. *Nat. Commun.* **2014**, *5*, 4195: 1-12.

(20) Park, C. H.; Schroeder, V.; Kim, B. J.; Swager, T. M. Ionic Liquid-Carbon Nanotube Sensor Arrays for Human Breath Related Volatile Organic Compounds. *ACS Sens.* **2018**, *3*, 2432-2437.

(21) Zeng, G.; Wu, C.; Chang, Y.; Zhou, C.; Chen, B.; Zhang, M.; Li, J.; Duan, X.; Yang, Q.; Pang, W. Detection and Discrimination of Volatile Organic Compounds using a Single Film Bulk Acoustic Wave Resonator with Temperature Modulation as a Multiparameter Virtual Sensor Array. *ACS Sens*. **2019**, *4*, 1524-1533.

(22) Wang, B.; Cancilla, J. C.; Torrecilla, J. S.; Haick, H. Artificial Sensing Intelligence with Silicon Nanowires for Ultraselective Detection in the Gas Phase. *Nano Lett.* **2014**, *14*, 933-938.

(23) Tonezzer, M.; Le, D. T. T.; Iannotta, S.; Van Hieu, N. Selective discrimination of hazardous gases using one single metal oxide resistive sensor. *Sens. Actuators, B* **2018**, *277*, 121-128.

(24) Shehada, N.; Brönstrup, G.; Funka, K.; Christiansen, S.; Leja, M.; Haick, H. Ultrasensitive Silicon Nanowire for Real-World Gas Sensing: Noninvasive Diagnosis of Cancer from Breath Volatolome. *Nano Lett.* **2014**, *15*, 1288-1295.

(25) Speller, N. C.; Siraj, N.; Regmi, B. P.; Marzoughi, H.; Neal, C.; Warner, I. M. Rational Design of QCM-D Virtual

Sensor Arrays Based on Film Thickness, Viscoelasticity, and Harmonics for Vapor Discrimination. *Anal. Chem.* **2015**, *87*, 5156-5166.

(26) Bur, C.; Bastuck, M.; Puglisi, D.; Schütze, A.; Lloyd Spetz, A.; Andersson, M. Discrimination and quantification of volatile organic compounds in the ppb-range with gas sensitive SiC-FETs using multivariate statistics. *Sens. Actuators, B* **2015**, *214*, 225-233.

(27) Potyrailo, R. A.; Bonam, R. K.; Hartley, J. G.; Starkey, T. A.; Vukusic, P.; Vasudev, M.; Bunning, T.; Naik, R. R.; Tang, Z.; Palacios, M. A.; Larsen, M.; Le Tarte, L. A.; Grande, J. C.; Zhong, S.; Deng, T. Towards outperforming conventional sensor arrays with fabricated individual photonic vapour sensors inspired by Morpho butterflies. *Nat. Commun.* **2015**, *6*, 7959: 1-12.

(28) Liu, H.; He, Y.; Nagashima, K.; Meng, G.; Dai, T.; Tong, B.; Deng, Z.; Wang, S.; Zhu, N.; Yanagida, T.; Fang, X. Discrimination of VOCs molecules via extracting concealed features from a temperature-modulated p-type NiO sensor. *Sens. Actuators, B* **2019**, *293*, 342-349.

(29) Tonezzer, M.; Kim, J.-H.; Lee, J.-H.; Iannotta, S.; Kim, S. S. Predictive gas sensor based on thermal fingerprints from Pt-SnO2 nanowires. *Sens. Actuators, B* **2019**, *281*, 670-678.

(30) Li, D.; Liu, G.; Zhang, Q.; Qu, M.; Fu, Y. Q.; Liu, Q.; Xie, J. Virtual sensor array based on MXene for selective detections of VOCs. *Sens. Actuators, B* **2021**, *331*, 129414: 1-9.

(31) Li, D.; Qu, M.; Zhang, Q.; Xie, J. Flexible Multivariable Sensor Based on Mxene and Laser-Induced Graphene for Detections of Volatile Organic Compounds in Exhaled Breath, *Proc. IEEE Int. Conf. Micro Electro Mech. Syst. MEMS*, 25-29 Jan. 2021, 482-485.

(32) Cheng, Y.; Ma, Y.; Li, L.; Zhu, M.; Yue, Y.; Liu, W.; Wang, L.; Jia, S.; Li, C.; Qi, T.; Wang, J.; Gao, Y. Bioinspired Microspines for a High-Performance Spray $T_{i3}C_2T_x$ MXene-Based Piezoresistive Sensor. *ACS Nano* **2020**, *14*, 2145-2155.

(33) Yagati, A. K.; Behrent, A.; Beck, S.; Rink, S.; Goepferich, A. M.; Min, J.; Lee, M.-H.; Baeumner, A. J. Laser-induced graphene interdigitated electrodes for label-free or nanolabel-enhanced highly sensitive capacitive aptamer-based biosensors. *Biosens. Bioelectron.* **2020**, *164,* 112272: 1-10.

(34) Ren, C. E.; Hatzell, K. B.; Alhabeb, M.; Ling, Z.; Mahmoud, K. A.; Gogotsi, Y. Charge- and Size-Selective Ion Sieving Through Ti3C2Tx MXene Membranes. *J. Phys. Chem. Lett.* **2015**, *6*, 4026-4031.

(35) Chen, W. Y.; Jiang, X.; Lai, S.-N.; Peroulis, D.; Stanciu, L. Nanohybrids of a MXene and transition metal dichalcogenide for selective detection of volatile organic compounds. *Nat. Commun.* **2020**, *11*, 1302: 1-10.

(36) Zhang, S.; Huang, P.; Wang, J.; Zhuang, Z.; Zhang, Z.; Han, W.-Q. Fast and Universal Solution-Phase Flocculation Strategy for Scalable Synthesis of Various Few-Layered MXene Powders. *J. Phys. Chem. Lett.* **2020,** *11*, 1247-1254.

(37) Muckley, E. S.; Naguib, M.; Ivanov, I. N. Multi-modal, ultrasensitive, wide-range humidity sensing with Ti3C2 film.

Nanoscale **2018**, *10*, 21689-21695.

(38) Potyrailo, R. A. Multivariable Sensors for Ubiquitous Monitoring of Gases in the Era of Internet of Things and Industrial *Internet. Chem. Rev.* **2016**, *116*, 11877-11923.

(39) Koh, H.-J.; Kim, S. J.; Maleski, K.; Cho, S.-Y.; Kim, Y.-J.; Ahn, C. W.; Gogotsi, Y.; Jung, H.-T. Enhanced Selectivity of MXene Gas Sensors through Metal Ion Intercalation: In Situ X-ray Diffraction Study. *ACS Sens.* **2019**, *4*, 1365-1372.

(40) Hayasaka, T.; Lin, A.; Copa, V. C.; Lopez, L. P.; Loberternos, R. A.; Ballesteros, L. I. M.; Kubota, Y.; Liu, Y.; Salvador, A. A.; Lin, L. An electronic nose using a single graphene FET and machine learning for water, methanol, and ethanol. *Microsys. Nanoeng.* **2020**, *6*, 50: 1-13.

(41) Gao, F.; Xuan, W.; Bermak, A.; Boussaid, F.; Tsui, C.-Y.; Luo, J. Dual transduction on a single sensor for gas identification. *Sens. Actuators, B* **2019**, *278*, 21-27.

(42) Guan, Y.; Le, X.; Hu, M.; Liu, W.; Xie, J. A noninvasive method for monitoring respiratory rate of rats based on a microcantilever resonant humidity sensor. *J. Micromech. Microeng.* **2019**, *29*, 125001: 1-8.

(43) Tipparaju, V. V.; Wang, D.; Yu, J.; Chen, F.; Tsow, F.; Forzani, E.; Tao, N.; Xian, X. Respiration pattern recognition by wearable mask device. *Biosens. Bioelectron.* **2020**, *169*, 112590:1-9.

(44) Jones, A. W.; Andersson, L. Comparison of ethanol concentrations in venous blood and end-expired breath during a controlled drinking study. *Forensic Sci. Int.* **2003**, *132*, 18-25.